

## Bayesian Modeling of Multiple Structural Connectivity Networks During the Progression of Alzheimer’s Disease

Christine B. Peterson<sup>1</sup>, Nathan Osborne<sup>2</sup>, Francesco C. Stingo<sup>3</sup>, Pierrick Bourgeat<sup>4</sup>,

James D. Doecke<sup>4</sup> and Marina Vannucci<sup>2,\*</sup>

<sup>1</sup>Department of Biostatistics, MD Anderson Cancer Center, Houston, TX, USA

<sup>2</sup>Department of Statistics, Rice University, Houston, TX, USA

<sup>3</sup>Department of Statistics, University of Florence, Italy

<sup>4</sup>Australian eHealth Research Centre, CSIRO Health and Biosecurity, Herston, QLD, Australia

\**email*: marina@rice.edu

**SUMMARY:** Alzheimer’s disease is the most common neurodegenerative disease. The aim of this study is to infer structural changes in brain connectivity resulting from disease progression using cortical thickness measurements from a cohort of participants who were either healthy control, or with mild cognitive impairment, or Alzheimer’s disease patients. For this purpose, we develop a novel approach for inference of multiple networks with related edge values across groups. Specifically, we infer a Gaussian graphical model for each group within a joint framework, where we rely on Bayesian hierarchical priors to link the precision matrix entries across groups. Our proposal differs from existing approaches in that it flexibly learns which groups have the most similar edge values, and accounts for the strength of connection (rather than only edge presence or absence) when sharing information across groups. Our results identify key alterations in structural connectivity which may reflect disruptions to the healthy brain, such as decreased connectivity within the occipital lobe with increasing disease severity. We also illustrate the proposed method through simulations, where we demonstrate its performance in structure learning and precision matrix estimation with respect to alternative approaches.

**KEY WORDS:** Alzheimer’s disease; Gaussian graphical model; AIBL study; MRI data; Bayesian inference

## **1. Introduction**

Dementia is a leading cause of death, disability, and health expenditure in the elderly, with Alzheimer's disease (AD) accounting for the majority of cases (Rowe et al., 2010). Much research in AD aims at understanding how the disease mechanisms affect the brain, in an effort to aid in the diagnosis and treatment of those with AD. Here we are interested in particular in exploring the changes in structural connectivity for different brain regions through the progression of the disease.

Traditional approaches to structural neuroimaging studies have focused on investigating cortical thickness, volume, and the rate of tissue loss as specific neurodegenerative biomarkers that relate to changes in the aging brain. More recently, attention has been given to the estimation of networks that capture the connectivity between cortical regions of interest and to the changes in connectivity that result from the progression of the neurological disease. It is widely known that correlated regions of interest are more likely to be part of a network or system, and that these networks are related to specific cognitive functions (Alexander-Bloch et al., 2013). During the progression of neurodegenerative disease, a person has a varying amount of cortical tissue loss, depending on their disease stage. As such the "connections" that are being assessed throughout the disease trajectory represent coordinated changes in brain tissue, which are reflected in cortical thickness measures. Many studies assess changes in structural connectivity via pairwise comparisons of cortical thickness (He et al., 2008; Alexander-Bloch et al., 2013; Pereira et al., 2016; Wang et al., 2016). However, while this can be effective in finding direct relationships between two areas, it does not assess the overall network of the functioning brain.

Statistical methods for network inference are a powerful tool to gain insight into the complex interactions that govern brain connectivity networks. When all samples are collected under similar conditions or reflect a single type of disease, methods such as the graphical lasso

(Meinshausen and Bühlmann, 2006; Yuan and Lin, 2007; Friedman et al., 2008) or Bayesian network inference approaches (Roverato, 2002; Wang, 2012; Wang and Li, 2012), among others, can be applied to infer a sparse graph and thereby learn the underlying network. These methods have been successfully used for the estimation of structural brain connectivity networks. For example, Huang et al. (2010) use the graphical lasso to demonstrate weaker between-lobe and weaker between-hemisphere connectivity for participants with AD versus healthy controls. Similarly, Ortiz et al. (2015) rely on graphical lasso methods to show a decrease in the amount of inter-region connectivity within the temporal lobe and increased connectivity within the frontal lobe in AD.

In studies where samples are obtained for different groups or subtypes of a disease, like the Australian Imaging, Biomarkers and Lifestyle (AIBL) study of ageing described below, separate estimation for each subgroup, as in Huang et al. (2010) and Ortiz et al. (2015), reduces statistical power by ignoring potential similarities across groups, while applying standard graphical model inference approaches to the pooled data across conditions leads to spurious findings. Recently, several estimation methods for multiple graphical models have been proposed in the statistical literature. Penalization-based approaches that encourage either common edge selection or precision matrix similarity by penalizing cross-group differences were proposed by Guo et al. (2011), Zhu et al. (2014), and Cai et al. (2015). Danaher et al. (2014) developed efficient convex penalization schemes designed to encourage similar edge values (the fused graphical lasso) or shared structure (the group graphical lasso), while Mohan et al. (2014) developed a penalization framework focused on similarity across networks as driven by the presence or absence of highly-connected hub nodes. More recent proposals encourage network similarity in a more tailored manner, assuming that the networks for each sample group are related within a tree structure (Oates and Mukherjee, 2014; Pierson et al., 2015), or, more generally, within an undirected weighted graph (Saegusa and Shojaie, 2016;

Ma and Michailidis, 2016). These methods assume that the relationships across groups are either known a priori or learned via hierarchical clustering. More flexible approaches that employ a Bayesian framework to simultaneously learn the networks for each group and the extent to which these networks are similar have been proposed in Peterson et al. (2015) and Shaddox et al. (2018). More specifically, Peterson et al. (2015) proposed representing the inclusion of edges using latent binary indicators, and the sharing of edges across groups was encouraged via a Markov random field prior linking the indicators. The prior on the precision matrix within each group was a  $G$ -Wishart distribution, which, given a graph structure  $G$ , restricts entries for missing edges to be exactly zero. While this approach is attractive since it enforces exact zeros in the precision matrix, its computational scalability is limited. Shaddox et al. (2018) improved upon Peterson et al. (2015) by replacing the  $G$ -Wishart prior with a mixture prior which is more amenable to efficient sampling. However, Shaddox et al. (2018) still addresses only the inclusion or exclusion of edges across groups, without consideration of edge strength or direction.

For the analyses of this paper, we propose a Bayesian Gaussian graphical modeling approach which retains the advantages of the approaches by Peterson et al. (2015) and Shaddox et al. (2018) in flexibly learning cross-group similarities within a joint framework, but that accounts for the similarity of edge values across groups, rather than only the binary presence or absence of those edges. Our framework allows us to not only learn the precision matrices within each group, but also to characterize the extent of shared edge values across the groups. Empirically, we demonstrate that this key feature results in a more accurate inference of the precision matrices. Unlike related approaches in the frequentist framework (Pierson et al., 2015; Saegusa and Shojaie, 2016), which require a separate, ad-hoc step to learn the cross-group relationships, we can simultaneously learn both the within-group and cross-group relationships. Furthermore, even though penalization based approaches are more scalable,

they provide only point estimates of large networks, which are often unstable given limited sample sizes. By taking a Bayesian approach, we are able to better quantify uncertainty in the estimates.

When applied to the data from the AIBL study, our method demonstrates that the majority of structural connections are preserved across all groups, but participants with AD have structural connectivity that is most unique compared to the other groups. In comparison to separate Bayesian estimation methods, the proposed method is able to identify a larger number of connections, reflecting the benefit of borrowing strength across groups. The fused graphical lasso, on the other hand, selects very dense graphs, that likely include a larger proportion of false positives edges, as also suggested by simulation studies.

The rest of the paper is organized as follows: We present the motivating AIBL study in Section 2. In Section 3 we describe in detail the proposed Bayesian joint graphical modeling approach and procedures for posterior inference. We return to the case study on AD in Section 4 and apply our method to estimate structural connectivity networks in subjects from cognitively normal to AD. Our results indicate structural changes in brain connectivity that occur as a result of the progression of the disease. In Section 5 we perform a simulation study to further illustrate the performance of our method with respect to alternative approaches. We conclude with a discussion in Section 6.

## **2. The AIBL study**

The main aim of the AIBL study was to recruit 1000 individuals over age 60 to enable prospective research into AD (Ellis et al., 2009). All subjects provided a blood sample, had cognitive testing, and completed health and lifestyle questionnaires, while a subset additionally underwent magnetic resonance imaging (MRI) brain imaging, positron emission tomography (PET) brain imaging, or activity monitoring.

Here, we focus on cortical thickness measurements from participants in the AIBL co-

hort who were either HC (healthy control), MCI (mild cognitive impairment) or had AD (Alzheimer’s disease). As a marker for neurodegeneration, cortical thickness is used to assess the atrophy of the cortical grey matter (GM) using MR images, and has been proposed as a more stable parameter for AD diagnosis than volume/density measures, because it is a more direct measure of GM atrophy (Singh et al., 2006; Li et al., 2012). Investigation into GM atrophy allows the approximate measurement of neuronal loss, which is one of the underlying hallmarks of neurodegenerative diseases. Analyses using cortical thickness have been shown to successfully separate AD from MCI and healthy control (Querbes et al., 2009). Our aim is to examine how the progression of AD affects the structural networks of the brain.

### 3. Proposed model

Here we introduce the proposed method, describing the likelihood, prior formulation, and an algorithm for posterior inference.

#### 3.1 Likelihood

Let  $K$  represent the number of sample groups (e.g., HC, MCI and AD) and let  $\mathbf{X}_k$  be the  $n_k \times p$  data matrix (e.g., cortical thickness on  $p$  brain regions) for the  $k$ th group, with  $k = 1, \dots, K$ . We assume that the observed values within each group arise from a multivariate normal distribution, where each row of  $\mathbf{X}_k$  corresponds to an independent observation following the distribution  $\mathcal{N}(\boldsymbol{\mu}_k, \boldsymbol{\Sigma}_k)$ . Since we are interested in the covariance structure, rather than the means, we assume that the data are centered by group, so that  $\boldsymbol{\mu}_k = \mathbf{0}_k$  for  $k = 1, \dots, K$ . The group-specific covariance matrix  $\boldsymbol{\Sigma}_k$  has inverse  $\boldsymbol{\Sigma}_k^{-1} = \boldsymbol{\Omega}_k \equiv (\omega_{k,ij})$ . The multivariate normal distribution has the special property that  $\omega_{ij} = 0$  if and only if variables  $i$  and  $j$  are conditionally independent given the remaining variables (Dempster, 1972). Non-zero entries in the precision matrix  $\boldsymbol{\Omega}_k$  therefore correspond to edges in the group-specific conditional

dependence graph  $G_k$ , which can be represented as a symmetric binary matrix where

$$g_{k,ij} = \begin{cases} 1 & \text{if edge } (i, j) \text{ is included in graph } k \\ 0 & \text{otherwise.} \end{cases}$$

In the Bayesian framework, inference of a graphical model is performed by tackling two interrelated sub-problems: selecting the model and learning the model parameters. Model selection is driven by identifying the graph structures  $G_k$ , while the precision matrices  $\mathbf{\Omega}_k$  are the key model parameters. Unlike many of the existing Bayesian approaches for multiple undirected graphical models, which are based on prior distributions that link groups through the graph structures  $G_k$ , in this paper we propose a novel prior that links the groups through the parameters  $\mathbf{\Omega}_k$ , accounting for edge strength rather than only edge presence or absence. The specification of such a prior requires some care as all precision matrices are constrained to be positive semidefinite.

### 3.2 Prior formulation

Our goal is to construct a prior on the precision matrices  $\mathbf{\Omega}_1 \dots, \mathbf{\Omega}_K$  that enables inference of a graphical model for each group, encourages similar edge values when appropriate, and allows for computationally tractable posterior inference. There have been a number of prior distributions proposed for the precision matrix  $\mathbf{\Omega}$  in a Gaussian graphical model. Early approaches required restrictive assumptions on the graph structure (in particular, decomposibility) to allow tractable sampling (Dawid and Lauritzen, 1993; Giudici and Green, 1999). Later methods included shrinkage priors (Wang, 2012), which offered computational scalability but not graph selection, and conjugate priors with no restriction on the graph structure (Roverato, 2002; Wang and Li, 2012), which, due to limited computational scalability, could only be applied in the moderate  $p$  setting.

Here, we build on the stochastic search structure learning (SSSL) model of Wang (2015), which assumes a normal mixture prior on the off-diagonal entries of the precision matrix,

enabling graph selection with no restrictions on the graph structure within a computationally efficient sampling framework. To achieve this, we define a joint prior distribution on the precision matrices  $\mathbf{\Omega}_1, \dots, \mathbf{\Omega}_K$  that encourages similarity across groups in terms of the off-diagonal elements of the precision matrices. Specifically, we consider the continuous shrinkage prior (Wang, 2012, 2015; Khondker et al., 2013) for  $K$  networks defined as

$$p(\mathbf{\Omega}_1, \dots, \mathbf{\Omega}_K | \{\mathbf{\Theta}_{ij} : i < j\}) \propto \prod_{i < j} \mathcal{N}_K(\boldsymbol{\omega}'_{ij} | \mathbf{0}, \mathbf{\Theta}_{ij}) \prod_i \prod_k \text{Exp}(\omega_{k,ii} | \lambda/2) \mathbf{1}_{\mathbf{\Omega}_1, \dots, \mathbf{\Omega}_K \in M^+}, \quad (1)$$

where  $\boldsymbol{\omega}_{ij} = (\omega_{1,ij}, \dots, \omega_{K,ij})$  is the vector of precision matrix entries corresponding to edge  $(i, j)$  across the  $K$  groups,  $\lambda > 0$  is a fixed hyperparameter, and  $M^+$  denotes the space of  $p \times p$  positive definite symmetric matrices. The first term in the joint prior specifies a multivariate normal prior with covariance matrix  $\mathbf{\Theta}_{ij}$  on the vector of precision matrix entries  $\boldsymbol{\omega}_{ij}$  corresponding to edge  $(i, j)$  across groups. To define a prior on  $\mathbf{\Theta}_{ij}$ , we work with the decomposition

$$\mathbf{\Theta}_{ij} = \text{diag}(\boldsymbol{\nu}_{ij}) \cdot \mathbf{\Phi} \cdot \text{diag}(\boldsymbol{\nu}_{ij}),$$

where  $\boldsymbol{\nu}_{ij}$  is a  $K \times 1$  vector of standard deviations specific to edge  $(i, j)$ , and  $\mathbf{\Phi}$  is a  $K \times K$  matrix shared across all  $(i, j)$  pairs with 1s along the diagonal. To ensure that  $\mathbf{\Theta}_{ij}$  is positive definite, the only requirements are that the standard deviations  $\nu_{k,ij}$  must be positive and  $\mathbf{\Phi}$  must be a valid correlation matrix. Given these constraints, we can then define a mixture prior on the edge-specific elements of  $\boldsymbol{\nu}_{ij}$  that enables the selection of edges in each graph, and a prior on the off-diagonal entries of  $\mathbf{\Phi}$  that allows us to model the relatedness of edge values across the sample groups. Following Wang (2015), the standard deviations  $\nu_{k,ij}$  are set to either a large or small value depending on whether edge  $(i, j)$  is included in graph  $k$ :

$$\nu_{k,ij} = \begin{cases} v_1 & \text{if } g_{k,ij} = 1 \\ v_0 & \text{otherwise.} \end{cases}$$

The hyperparameters  $v_1 > 0$  and  $v_0 > 0$  are fixed to large and small values, respectively. Small values of  $v_0$  will shrink the value of  $\omega_{k,ij}$  for edges which are not included in the



graph towards 0. This prior indirectly encourages the selection of similar graphs in related networks. Specifically, a small value of  $\omega_{k,ij}$  will encourage small values of  $\omega_{l,ij}$  for any other group  $l$  and in turn the exclusion of edge  $(i, j)$  in both groups  $k$  and  $l$ . Similarly, a large value of  $\omega_{k,ij}$  will encourage large values of  $\omega_{l,ij}$  and the inclusion of edge  $(i, j)$  in groups  $k$  and  $l$ . Networks  $k$  and  $l$  are considered related if the posterior distribution of the  $(k, l)$  element of  $\Phi$  is concentrated on relatively larger values.

For the prior on the graphs  $G_1, \dots, G_K$ , we assume an independent Bernoulli distribution

$$p(G_1, \dots, G_K) \propto \prod_{k=1}^K \prod_{i < j} \{ \pi^{g_{k,ij}} (1 - \pi)^{1 - g_{k,ij}} \}. \quad (2)$$

This prior is analytically defined only up to a normalizing constant. As discussed in Wang (2015), the unknown normalizing constant of prior (1) and prior (2) are proportional and cancel out in the joint prior on  $(\Omega_k, G_k)$ . Consequently, the parameter  $\pi$  is not exactly the prior probability of edge inclusion; however, as shown by Wang (2015) the effect of these unknown normalizing constants on the posterior inference is extremely mild, and the parameter  $\pi$  can be easily calibrated to achieve a pre-specified level of sparsity.

Recall that  $\Phi$  is a correlation matrix, and must therefore have all diagonal entries fixed to 1 and be positive definite. To specify the prior on  $\Phi$ , we rely on the joint uniform prior proposed in Barnard et al. (2000):

$$p(\Phi) \propto 1 \cdot \mathbf{1}_{\Phi \in \mathcal{R}^K}, \quad (3)$$

where  $\mathcal{R}^K$  denotes the space of valid  $K \times K$  correlation matrices i.e. positive definite symmetric matrices  $\Phi$  such that  $\phi_{jk} = 1$  for all  $j = k$  and  $|\phi_{jk}| < 1$  for all  $j \neq k$ . When  $\Phi = \mathbf{I}$ , the precision matrices for each group are independent, and the proposed model reduces to that of Wang (2015) applied separately to each sample group.

Alternative priors could be defined on the precision matrices  $\Omega_1, \dots, \Omega_K$  that ensure the support to be constrained to the space of symmetric positive semidefinite matrices  $M^+$ . However, our proposed prior has the key advantage of computational tractability. In the next

section we show how we can define a sampler that is automatically restricted to the targeted support  $M^+$ . In our model cross-group similarity is defined by the parameter  $\Phi$  that links the elements of the precision matrices, whereas previous Bayesian approaches (Peterson et al., 2015; Shaddox et al., 2018) encouraged similarity through a joint prior on the adjacency matrices  $G_1, \dots, G_K$ .

### 3.3 MCMC algorithm for posterior inference

Given the likelihood and priors defined above, the full joint posterior can be written as

$$p(\Omega_1, \dots, \Omega_K, G_1, \dots, G_K, \Phi | \mathbf{X}_1, \dots, \mathbf{X}_K) \propto \left[ \prod_{k=1}^K p(\mathbf{X}_k | \Omega_k) \right] \cdot p(\Omega_1, \dots, \Omega_K | G_1, \dots, G_K, \Phi) \cdot p(G_1, \dots, G_K) \cdot p(\Phi),$$

where we re-express the prior  $p(\Omega_1, \dots, \Omega_k | \{\Theta_{ij} : i < j\})$  defined in equation (1) as  $p(\Omega_1, \dots, \Omega_k | G_1, \dots, G_k, \Phi)$  since  $\{\Theta_{ij} : i < j\}$  is completely determined by  $G_1, \dots, G_k$  and  $\Phi$ . Since the posterior distribution is analytically intractable, we rely on Markov chain Monte Carlo (MCMC) sampling to generate a sample of the parameters for the purposes of posterior inference. The overall scheme is a Gibbs sampler, with parameters sampled from their full conditional distributions in each iteration, given the data and the parameter values from the previous iteration. At a high level, the sampling steps are as follows:

- **Step 1:** For each sample group  $k = 1, \dots, K$ , we first update the precision matrix  $\Omega_k$  using a block Gibbs sampler, and then the graph  $G_k$  by drawing each edge from an independent Bernoulli. To update  $\Omega_k$ , we follow an efficient sampling scheme utilizing closed-form conditional distributions for each column, based on the approach in Wang (2015). Specifically, to update the final row/column of  $\Omega_k$ , we perform a change of variables  $(\omega_{k,1p}, \omega_{k,pp}) \rightarrow (\mathbf{u}, v)$  - with  $\omega_{k,1p}$  being a vector that comprises the first  $p - 1$  elements of the final column of  $\Omega_k$  -, and sample the auxiliary variables  $\mathbf{u}$  and  $v$  from the product of a gamma and a multivariate normal distribution, conditional on the data and current

values of the remaining parameters:

$$(\mathbf{u}, v) | \cdot \sim \text{Gamma}\left(\frac{n_K}{2} + 1, \frac{s_{K,22} + \lambda}{2}\right) \mathcal{N}(\mathbf{C}\mathbf{a}, \mathbf{C}),$$

where the parameters of the gamma and normal are defined in the Supplementary Material. The auxiliary variables  $\mathbf{u}$  and  $v$  are then mapped via a one-to-one transformation to the updated values for the final row/column of  $\mathbf{\Omega}_k$ . The remaining columns are updated similarly. The graph  $G_k$  is updated entry-wise by sampling from the Bernoulli distribution with probability:

$$p(g_{k,ij} = 1 | \mathbf{\Omega}_k, \mathbf{X}_k) = \frac{\mathcal{N}(\omega_{k,ij} | 0, \nu_1^2) \pi}{\mathcal{N}(\omega_{k,ij} | 0, \nu_1^2) \pi + \mathcal{N}(\omega_{k,ij} | 0, \nu_0^2) (1 - \pi)}.$$

- **Step 2:** Sample the entire correlation matrix  $\mathbf{\Phi}$  at once using a Metropolis-within-Gibbs step following the parameter expansion method of Liu and Daniels (2006). Specifically, we first sample a covariance matrix  $\mathbf{\Psi}$  from the inverse-Wishart distribution:

$$\mathbf{\Psi} | \cdot \sim \mathcal{W}^{-1}\left(\sum_{i < j} \text{diag}(\boldsymbol{\nu}_{ij})^{-1} \boldsymbol{\epsilon}_{ij} \boldsymbol{\epsilon}'_{ij} \text{diag}(\boldsymbol{\nu}_{ij})^{-1}, p(p-1)/2\right),$$

where the parameters are as defined in the Supplementary Material. This covariance matrix is then mapped to a proposal for the correlation matrix  $\mathbf{\Phi}^*$  via a reduction function, and accepted with probability:

$$\alpha = \min \left\{ 1, \exp \left( (K+1)/2 \cdot (\log |\mathbf{\Phi}^*| - \log |\mathbf{\Phi}|) \right) \right\}.$$

Additional details on the two steps above are given in the Supplementary Material. After discarding the results from the burn-in period, we take the median model (Barbieri and Berger, 2004) as the posterior selected value for the graph  $G_k$  for each group. Specifically, we select edges  $g_{k,ij}$  with marginal posterior probability of inclusion  $\geq 0.5$ , the same criterion as in Wang (2015). To obtain a posterior estimate of the precision matrix consistent with the posterior selected graph, we resample  $\mathbf{\Omega}_k$  conditional on the posterior estimate of  $\mathbf{\Phi}$  and selected value of  $G_k$  for  $k = 1, \dots, K$ .

## 4. Structural connectivity patterns in the AIBL cohort

### 4.1 Subjects and MRI data processing

We have disease stage information and measurements of cortical thickness across 100 regions of interest in the brain from a total of 584 subjects. Here we focus on imaging data and cognitive assessments from the last follow up time point available. The subjects were divided into four groups: high performing HC (hpHC,  $n=143$ ), HC ( $n=145$ ), MCI ( $n=148$ ), and AD ( $n=148$ ). To obtain this classification, subjects were first evaluated by a clinician for current diagnosis and categorized as HC, MCI, or AD. HC subjects were further divided into hpHC and HC using eight different cognitive composite scores representing different cognitive domains. Each cognitive composite score was used to estimate group classification (hpHC/HC) using latent class regression with finite mixture models.

All subjects received T1 weighted magnetic resonance imaging (MRI) using the ADNI 3-dimensional (3D) Magnetization Prepared Rapid Gradient Echo (MPRAGE) sequence, with 11 mm in-plane resolution and 1.2 mm slice thickness, TR/TE/T1 2300/2.98/900, flip angle 9 (degree), and field of view  $240 \times 256$  and 160 slices (Rowe et al., 2010). Each image was first segmented into grey matter (GM), white matter, and cerebrospinal fluid (CSF) using an implementation of the expectation maximization algorithm (Leemput et al., 1999). Using the GM segmentation, cortical thickness was computed via a combined Lagrangian-Eulerian PDE approach (Acosta et al., 2009). The cortex was parcellated into a set of 100 regions of interest (ROI), obtained by segmentation propagation using the Neuromorphometrics atlas (<http://www.neuromorphometrics.com>). A list of ROIs, grouped by lobe of the brain, is given in Table S1 in the Supplementary Material. Mean cortical thickness was computed in each ROI, and used in subsequent analysis. This gave us data on  $p = 100$  brain regions for the  $K = 4$  groups of subjects. Within each group, data were centered.

#### 4.2 Application of the proposed method

The application of our model requires the specification of a few hyperparameters. Here we provide details on the specification we used to obtain the results reported below and refer readers to the sensitivity analysis found in the Supplementary Material for more insights on parameter selection. In particular, priors (1) and (2) require the choice of the hyperparameters  $\nu_0$ ,  $\nu_1$ , and  $\pi$ . These were set to  $\nu_0 = 0.01$ ,  $\nu_1 = 15$ , and  $\pi = \frac{2}{(100-1)}$ . The parameters  $\nu_0$  and  $\nu_1$  were chosen so that the network structure results were sparse, while the selection of  $\pi$  was based on the default setting recommended in Wang (2015). As a guideline, increasing  $\nu_0$  while holding the ratio between  $\nu_0$  and  $\nu_1$  fixed will result in sparser graphs, as shown in the sensitivity analysis, which agrees with the sensitivity analysis provided in Wang (2015). Increasing the ratio between  $\nu_0$  and  $\nu_1$  while holding  $\nu_0$  fixed will likewise increase the sparsity of the inferred graphs.

The results we report below were obtained by running two MCMC chains with 20,000 iterations, after a burn-in of 5,000 iterations. Posterior probabilities of inclusion (PPI) for each edge were compared for the two chains to check for convergence. A correlation of 0.997 was found between these two posterior samples. We also used the Gelman and Rubin's convergence diagnostic (Gelman and Rubin, 1992) to check for signs of non-convergence of the individual parameters of the estimated  $\Phi$  matrix and the estimated precision matrices. Those statistics were all below 1.1, clearly indicating that the MCMC chains were run for a sufficient number of iterations. The results reported here were obtained by pooling together the outputs from the two chains to give a total of 20,000 MCMC samples.

#### 4.3 Results

Figure 1 shows histograms of the PPIs for each group and scatter plots of the PPIs across pairs of groups. Off-diagonal plots show scatter plots of the PPIs, on the upper triangle plots, and percents of PPIs falling in each quadrant, in the lower triangle plots, for pairs of groups.

In the scatter plots, the points in the upper right quadrants indicate edges that belong to the median model in both groups (shared edges), while points in the lower right and upper left quadrants indicate edges that were selected in one group but not the other (differential edges). The points in the lower left quadrant correspond to edges selected in neither group. These plots illustrate that the edge selection is fairly sparse overall, with a high concentration of PPIs close to 0 in the histograms, and that there are a number of edges which are strongly supported as shared across groups, as shown by the dense cluster of points in the upper right corner of the off-diagonal plots. Finally, we can see that many of the PPI values are the same across groups, as shown in the linear trend in the upper triangle plots. From these plots, we can also see that AD differentiates itself from the other groups most, because of the PPI values that vary greatly (far away from the linear trend) from AD and the other groups. Additionally, heatmaps of the PPIs within each group are shown in Figure 2. In these plots, the ROIs are groups within brain lobes, specifically, frontal, temporal, parietal, occipital and limbic cortex. As expected, larger PPIs values are observed within lobes vs. across lobes for all disease stages.

[Figure 1 about here.]

[Figure 2 about here.]

To allow an in-depth view of the estimated networks, subnetworks corresponding to the individual lobes are shown in Figure 3, where the edges shown are those selected in the median model; the estimated graphs  $G_k$  for each group across all lobes are plotted in Supplementary Figure S2. In these circular plots, the left side represents the left brain hemisphere, and the right side represents the right brain hemisphere. In all plots, blue lines indicate edges shared by all 4 groups, red lines indicate edges unique to an individual group, and black lines those shared by 2 or more groups. The strongest pattern visible in the graphs are the horizontal blue lines connecting the corresponding regions in the right and left hemispheres of the brain.

The pattern of strong correlations between contralateral homologous regions of the cortex in structural imaging has been previously observed, for example by Mechelli et al. (2005).

Our findings are quantified in Table 1, which summarizes the numbers of edges included per group and shared across groups in the networks for all ROIs of Supplementary Figure S2 and the lobe-specific networks of Figure 3. Within each subtable, the diagonal values represent the numbers of edges present in each group, and the off-diagonal values are the numbers of shared edges between pairs of groups. Finally, the numbers of edges which are unique to a specific group is reported as values in parenthesis along the diagonals. From this, we see that the healthy control groups have slightly more edges than the cognitively impaired groups. We can also see that there is a decrease in connections in the occipital lobe as AD progresses.

Additional ROI-specific patterns can be derived from Table S2 in the Supplementary Material, which reports the total number of edges for each ROI pair, across the four groups. For example, the Calcerine Cortex shows a decrease in edges in the MCI and AD groups and the AD group shows the most connections in the Amygdala.

[Figure 3 about here.]

[Table 1 about here.]

Our method also produces estimated values of the elements of the  $\Phi$  matrix, which capture similarity in the precision matrix entries between the different subject groups:

$$\begin{pmatrix} & \text{hpHC} & \text{HC} & \text{MCI} & \text{AD} \\ \text{hpHC} & 1.000 & & & \\ \text{HC} & 0.929 & 1.000 & & \\ \text{MCI} & 0.942 & 0.885 & 1.000 & \\ \text{AD} & 0.865 & 0.940 & 0.883 & 1.000 \end{pmatrix}$$

These values, which reflect the similarity in edge strength across groups, provide a com-

plementary look at the patterns of structural connectivity. In particular, the values of  $\Phi$  show that the hpHC and AD groups are the least similar. They also show that HC and AD are related, which is supplemented by Table 1 which shows that HC and AD have a large number of shared edges. The similarity of HC and AD may be caused by the way hpHC and HC were separated from each other, as HC may have a higher propensity to develop AD. These findings illustrate that there may be an underlying classification other than AD that influences the structural connectivity.

We conclude our analysis by summarizing the network structure of the estimated graphs via some graph metrics commonly used in neuroimaging (Yao et al., 2010). Specifically, we calculated the clustering coefficient  $\gamma$ , the absolute path length  $\lambda$ , and the small world coefficient  $\sigma = \gamma/\lambda$ . See Yao et al. (2010), and references within, for a formal definition. These measurements are used to describe small-world properties of a network, where small values of  $\lambda$  ( $\approx 1$ ) and larger values of  $\gamma$  ( $> 1$ ) may indicate a higher speed of information dissemination and more efficient information processing (Sporns and Zwi, 2004). If both  $\lambda \approx 1$  and  $\gamma > 1$ , and consequently  $\sigma > 1$ , a network is said to exhibit small-world characteristics. Disconnected nodes were removed when calculating the characteristic path length. Based on the estimated values of  $\lambda$  and  $\gamma$ , we obtain small world coefficients  $\sigma$  of 1.717, 1.635, 1.627, and 1.475 for hpHC, HC, MCI, and AD, respectively. We observe that  $\sigma$  is greater than 1 for all the groups, but steadily decreases during the progression of AD. Small-world characteristics in the brain network of AD have also observed by other authors (He et al., 2008)

#### 4.4 Results from alternative approaches

To provide additional perspective, we compare our edge selection results to those of separate graph estimation in the Bayesian framework (Wang, 2015) and the fused graphical lasso (Danaher et al., 2014). These methods are particularly relevant for comparison as separate Bayesian estimation provides insight on the impact of the prior linking the groups, while



the fused graphical lasso is the most popular frequentist method for estimation of multiple graphs accounting for similarity in edge values. Separate Bayesian inference was applied using the same settings for  $\nu_0$ ,  $\nu_1$ ,  $\lambda$ , and  $\pi$  as in the linked method. For the fused graphical lasso,  $\lambda_1$  and  $\lambda_2$  were selected by performing a grid search to find the combination of values minimizing the AIC, as recommended in Danaher et al. (2014).

For each of the brain regions, Table 2 shows the number of total edges for each method on the diagonal, and the number of common edges on the off-diagonal. Although the ground truth is not known, these results suggest that the proposed linked precision matrix method generally improves power over separate estimation: a large majority of the edges selected using separate estimation are also discovered under the proposed method, while separate estimation results in an overly sharp increase in the number of edges across stages. We see a similarly large overlap of selected edges with the joint Bayesian estimation, though the joint Bayesian method leads to models that are more dense, due, in part, to the larger number of parameters of that model that control the sparsity. The fused graphical lasso tends to select models which are even denser. This is because the AIC is not optimal for variable selection, tending to result in models which are not sufficiently sparse. The Bayesian separate estimation method showed connectivity trends contrary to those found in Alexander-Bloch et al. (2013), namely, connectivity increases with the progression of AD using this method. Finally, as discussed in Section 4.3, the proposed linked precision matrix provides an additional summary of cross-group similarity (in the form of the  $\Phi$  matrix) which is not available under the other methods.

[Table 2 about here.]

## 5. Simulation study

We present here a simulation study designed to allow a comparison of performance across methods in learning graphs with related structure. The simulation is designed to mimic the real data application in terms of the number of variables, number of subjects per group, and graph structures.

We consider a setting with  $K = 3$  groups,  $p = 100$  variables, and  $n = 150$  observations per group, where the underlying graph and precision matrix for each group are constructed as follows.  $G_1$ , the graph for the first group, consists of 5 communities, each with 20 variables. Within each community, the nodes are connected via a scale-free network. There are no connections across communities in  $G_1$ . The precision matrix entries in  $\mathbf{\Omega}_1$  for edges are sampled independently from the uniform distribution on  $[-0.6, -0.4] \cup [0.4, 0.6]$ , while entries for missing edges are set to 0. To obtain  $G_2$ , five edges are removed from  $G_1$  and five new edges added at random, so that now there are some cross-community connections. The entries in  $\mathbf{\Omega}_2$  for the new edges are generated in a similar fashion as for  $\mathbf{\Omega}_1$ , while the entries for the edges removed are set to zero. To ensure positive definiteness,  $\mathbf{\Omega}_1$  and  $\mathbf{\Omega}_2$  are each adjusted following the approach in Danaher et al. (2014). To obtain  $G_3$ , 20 edges are removed from the graph for group 2, and the corresponding 20 entries in  $\mathbf{\Omega}_2$  are set to zero to obtain  $\mathbf{\Omega}_3$ . These steps result in graphs  $G_1$  and  $G_2$  that share 180 of 185 edges (97.3%), graphs  $G_2$  and  $G_3$  that share 165 of 185 edges (89.2%), and graphs  $G_1$  and  $G_3$  that share 162 of the 185 edges in  $G_1$  (87.6%). The correlations between the off-diagonal elements of the precision matrices are 0.98 between  $\mathbf{\Omega}_1$  and  $\mathbf{\Omega}_2$ , 0.94 between  $\mathbf{\Omega}_2$  and  $\mathbf{\Omega}_3$ , and 0.93 between  $\mathbf{\Omega}_1$  and  $\mathbf{\Omega}_3$ . To simulate the data, we generate  $n$  samples per group from the multivariate normal distribution  $\mathcal{N}(0, \mathbf{\Omega}_k^{-1})$ , for  $k = 1, 2, 3$ . Below we report results obtained over 25 simulated data sets.

### 5.1 Performance comparison

We compare the following methods: fused graphical lasso (Danaher et al., 2014), group graphical lasso (Danaher et al., 2014), Bayesian inference applied separately for each group (Wang, 2015), Bayesian joint inference relating edge probabilities (Shaddox et al., 2018), and the proposed Bayesian joint inference method linking the precision matrix entries. For the lasso methods, the within-group penalty  $\lambda_1$  and cross-group penalty  $\lambda_2$  were selected using a grid search to identify the combination that minimize the AIC. Both separate Bayesian inference and the proposed linked precision matrix approach were applied using the parameter setting  $\nu_0 = 0.01$ ,  $\nu_1 = 0.1$ ,  $\lambda = 1$ , and  $\pi = 2/(p - 1)$ . Shaddox et al. (2018) was applied using  $\nu_0 = 0.05$ ,  $\nu_1 = 0.5$ ,  $\lambda = 1$ ,  $a = 1$ ,  $b = 16$ ,  $\alpha = 2$ ,  $\beta = 5$ , and  $w = 0.5$ , where the parameters were chosen to achieve a similar number of selected edges as obtained under the proposed linked precision matrix approach.

All Bayesian methods were run with 10,000 iterations as burn-in and 20,000 iterations as the basis for posterior inference. For the Bayesian methods, we take the posterior selected graph as the median model, and we compute the posterior estimate of the precision matrices  $\Omega_k$  as the MCMC average when the precision matrices are resampled conditional on the graphs and the posterior estimate of  $\Phi$  from the initial run (for the proposed method), or conditional on the graph using separate mixture priors (for the separate and joint estimation approaches).

The performance across methods in terms of edge selection and differential edge selection is compared on the basis of the true positive rate (TPR), the false positive rate (FPR), the Matthews correlation coefficient (MCC), and area under the curve (AUC). The performance of precision matrix estimation is compared using the Frobenius loss between the true precision matrix and the estimated precision matrix. Following Guo et al. (2011), this loss is defined

as

$$FL = \frac{1}{K} \sum_{k=1}^K \|\Omega_k - \hat{\Omega}_k\|_F^2 / \|\Omega_k\|_F^2,$$

where  $\|\cdot\|_F$  denotes the Frobenius norm. For the lasso methods, the AUC of edge selection was computed by fixing the cross-group penalty parameter  $\lambda_2$ , and then varying the within-group penalty parameter. This was repeated for a range of  $\lambda_2$  values, and the best AUC was kept. For the Bayesian methods, the AUC of edge selection was computed by varying the threshold on the posterior probabilities of inclusion from 0 to 1. For differential edge selection using the Bayesian methods, a posterior probability of difference for each pair of edges was computed based on the MCMC sample, following the same procedure as in Peterson et al. (2015). Specifically, for edge  $(i, j)$ , the posterior probability of being differential between graphs  $k$  and  $m$  is computed as the MCMC average  $\frac{1}{T} \sum_{t=1}^T |g_{k,ij}^{(t)} - g_{m,ij}^{(t)}|$ . This PPI of difference was thresholded at 0.5 for computing the TPR, FPR, and MCC, and the threshold on this PPI was varied from 0 to 1 to compute the AUC.

The performance results for graph and precision matrix learning are given in Table 3. In general, the Bayesian methods tend to favor sparser graphs, and achieve quite low false positive rates. The lasso methods tend to select somewhat denser graphs, and have correspondingly higher TPRs and FPRs. The proposed linked precision matrix method achieves the best overall performance, as demonstrated by its high MCC value (a balanced measure of classification accuracy given a single selected model). The AUC, which is computed across a range of model sizes, shows that the lasso methods and the proposed linked precision matrix approach have very good accuracy. For the lasso methods, the AUC was computed for multiple values of the cross-group penalty parameter while varying the within-group penalty, and the best was included here. Thus, the reported AUCs for these methods are likely to err on the optimistic side. Finally, the Frobenius loss (which reflects the accuracy of the precision matrix estimation) is minimized under the proposed method.

[Table 3 about here.]

Based on the results in Table 3, the proposed method is conservative in the identification of differential edges, as indicated by its fairly low sensitivity and very high specificity. The proposed method achieves both the highest MCC and AUC across methods compared. The high false positive rate of the lasso methods in selecting differential edges is partly due to the fact that they select a larger number of false positive edges overall, and may also reflect that they use a single penalty parameter to control cross-group similarity, which is not optimal when some groups have more similar dependence structure than others.

Finally, the proposed linked precision matrix approach provides a posterior summary of cross-group similarity. Specifically, the posterior estimated value of  $\Phi$  under the proposed linked precision matrix method is

$$\begin{pmatrix} 1.0 & 0.65 & 0.63 \\ & 1.0 & 0.64 \\ & & 1.0 \end{pmatrix}.$$

Although the entries are fairly similar across groups, we can see that groups 1 and 2, which are the most similar to each other, have a higher value in the  $\Phi$  matrix.

Additional simulation scenarios with varying degrees of shared structure and edge values are included in Section S4 of the supplementary material. These simulations demonstrate that although the proposed method has the largest performance advantage when edge values across groups are in fact similar, it is robust to deviations from this setting, and performs similarly to separate Bayesian inference when there is no more overlap across groups than by random chance.

## 6. Discussion

We have introduced a novel method for the joint analysis of multiple brain networks. The proposed approach allows flexible modeling of the cross-group relationships, resulting in

relative measures of precision matrix similarity which fall in the  $(0, 1)$  interval. Additionally, the proposed model improves on other methods for joint estimation in that it not only shares information about the presence or absence of edges between groups, but also shares information about the strength of those connections. These two novel features provide more in depth inference, as  $\Phi$  provides a measure of the relatedness of the groups, and accurate estimation of both network structures and precision matrices as shown in the simulation studies. Building on the sampling framework laid out by Wang (2015) allows the proposed method to be scalable; the posterior sampling for a data set comprised of  $p = 100$  ROIs and  $K = 4$  groups took approximately 55 minutes for 1000 MCMC iterations in MATLAB on a laptop with a single Intel(R) Core(TM) i5-5200U CPU @ 2.20GHz and 16GB RAM. The proposed method was proven to be suitable for the analysis of multiple brain networks based on ROI measurements; in case the interest is in larger networks, such as networks of voxels, more scalable approaches should be used.

We have applied our method to the analysis of structural data from the AIBL study on Alzheimer’s disease, with the purpose of exploring the changes in structural connectivity for different brain regions through the progression of the disease. Our method has demonstrated that the majority of structural connections are preserved across all groups. Some of our findings are consistent with the literature on structural connectivity networks in Alzheimer patients: networks are fairly sparse and a number of edges are shared across groups.

In theory, structural connectivity networks in Alzheimer’s patients do not change dramatically with disease progression. Our findings confirm this theory, and support our assumption that all networks are similar to some extent, i.e. all elements of the  $\Phi$  matrix are non-zero. However, from a statistical modeling perspective, it might be of interest to replace the prior given in equation (3) with a prior that assumes sparsity of the cross-group relationships. Such an extension is non-trivial due to the combination of constraints that  $\Phi$  must both

be a positive-definite matrix and have all diagonal entries fixed to 1. Existing sampling approaches in this context either assume specific priors which are not suitable to the current context (Chan and Jeliaskov, 2009) or allow arbitrary priors, but lack scalability (Barnard et al., 2000). Efficient procedures for sampling sparse correlation matrices is therefore a topic of interest for future work.

## References

- Acosta, O., Bourgeat, P., Zuluaga, M. A., Fripp, J., Salvado, O., and Ourselin, S. (2009). Automated voxel-based 3D cortical thickness measurement in a combined Lagrangian-Eulerian PDE approach using partial volume maps. *Med. Image Anal.* **13**, 730 – 743.
- Alexander-Bloch, A., Giedd, J. N., and Bullmore, E. (2013). Imaging structural co-variance between human brain regions. *Nat. Rev. Neurosci.* **14**, 322–336.
- Barbieri, M. and Berger, J. (2004). Optimal predictive model selection. *Ann. Stat.* **32**, 870–897.
- Barnard, J., McCulloch, R., and Meng, X. (2000). Modeling covariance matrices in terms of standard deviations and correlations, with application to shrinkage. *Stat. Sinica* **10**, 1281–1311.
- Cai, T., Li, H., Liu, W., and Xie, J. (2015). Joint estimation of multiple high-dimensional precision matrices. *Stat. Sinica* **38**, 2118–2144.
- Chan, J. and Jeliaskov, I. (2009). MCMC estimation of restricted covariance matrices. *J. Comput. Graph. Stat.* **18**, 457–480.
- Danaher, P., Wang, P., and Witten, D. (2014). The joint graphical lasso for inverse covariance estimation across multiple classes. *J. R. Stat. Soc. B* **76**, 373–397.
- Dawid, A. and Lauritzen, S. (1993). Hyper Markov laws in the statistical analysis of decomposable graphical models. *Ann. Stat.* **21**, 1272–1317.
- Dempster, A. (1972). Covariance selection. *Biometrics* **28**, 157–175.

- Ellis, K. A., Bush, A. I., Darby, D., De Fazio, D., Foster, J., Hudson, P., et al. (2009). The Australian Imaging, Biomarkers and Lifestyle (AIBL) study of aging: methodology and baseline characteristics of 1112 individuals recruited for a longitudinal study of Alzheimer's disease. Int. Psychogeriatr. **21**, 672–687.
- Friedman, J., Hastie, T., and Tibshirani, R. (2008). Sparse inverse covariance estimation with the graphical lasso. Biostatistics **9**, 432–441.
- Gelman, A. and Rubin, D. B. (1992). Inference from iterative simulation using multiple sequences. Stat. Sci. **7**, 457–472.
- Giudici, P. and Green, P. J. (1999). Decomposable graphical Gaussian model determination. Biometrika **86**, 785–801.
- Guo, J., Levina, E., Michailidis, G., and Zhu, J. (2011). Joint estimation of multiple graphical models. Biometrika **98**, 1–15.
- He, Y., Chen, Z., and Evans, A. (2008). Structural insights into aberrant topological patterns of large-scale cortical networks in Alzheimer's disease. J. Neurosci. **28** **18**, 4756–66.
- Huang, S., Li, J., Sun, L., Ye, J., Fleisher, A., Wu, T., et al. (2010). Learning brain connectivity of Alzheimer's disease by sparse inverse covariance estimation. NeuroImage **50**, 935 – 949.
- Khondker, Z., Zhu, H., Chu, H., Lin, W., and Ibrahim, J. (2013). Bayesian covariance lasso. Stat. Interface **6**, 243–259.
- Leemput, K. V., Maes, F., Vandermeulen, D., and Suetens, P. (1999). Automated model-based tissue classification of MR images of the brain. IEEE T. Med. Imaging **18**, 897–908.
- Li, Y., Wang, Y., Wu, G., Shi, F., Zhou, L., Lin, W., and Shen, D. (2012). Discriminant analysis of longitudinal cortical thickness changes in Alzheimer's disease using dynamic and network features. Neurobiol. Aging **33**,
- Liu, X. and Daniels, M. (2006). A new algorithm for simulating a correlation matrix based



- on parameter expansion and reparameterization. J. Comput. Graph. Stat. **15**, 897–914.
- Ma, J. and Michailidis, G. (2016). Joint structural estimation of multiple graphical models. J. Mach. Learn. Res. **17**, 1–48.
- Mechelli, A., Friston, K. J., Frackowiak, R. S., and Price, C. J. (2005). Structural covariance in the human cortex. J. Neurosci. **25**, 8303–8310.
- Meinshausen, N. and Bühlmann, P. (2006). High-dimensional graphs and variable selection with the lasso. Ann. Statist. **34**, 1436–1462.
- Mohan, K., London, P., Fazel, M., Witten, D., and Lee, S. (2014). Node-based learning of multiple Gaussian graphical models. J. Mach. Learn. Res. **15**, 445–488.
- Oates, C. and Mukherjee, S. (2014). Joint structure learning of multiple non-exchangeable networks. Proceedings of the 17th International Conference on Artificial Intelligence and Statistics (AISTATS) **33**,.
- Ortiz, A., Munilla, J., Álvarez-Illán, I., Górriz, J., Ramírez, J., and The Alzheimer’s Disease Neuroimaging Initiative (2015). Exploratory graphical models of functional and structural connectivity patterns for Alzheimer’s disease diagnosis. Front. Comp. Neurosc. **9**, 132.
- Pereira, J. B., Mijalkov, M., Kakaei, E., Mecocci, P., Vellas, B., Tsolaki, M., et al. (2016). Disrupted network topology in patients with stable and progressive mild cognitive impairment and Alzheimer’s disease. Cerebral Cortex **26**, 3476–3493.
- Peterson, C. B., Stingo, F., and Vannucci, M. (2015). Bayesian inference of multiple Gaussian graphical models. J. Am. Stat. Assoc. **110**, 159–174.
- Pierson, E., Consortium, G., Koller, D., Battle, A., and Mostafavi, S. (2015). Sharing and specificity of co-expression networks across 35 human tissues. PLOS Comput. Biol. **11**,.
- Querbes, O., Aubry, F., Pariente, J., Lotterie, J., Démonet, J.-F., Duret, V., et al. (2009). Early diagnosis of Alzheimer’s disease using cortical thickness: impact of cognitive

- reserve. Brain **132**, 2036–2047.
- Roverato, A. (2002). Hyper inverse Wishart distribution for non-decomposable graphs and its application to Bayesian inference for Gaussian graphical models. Scand. J. Statist. **29**, 391–411.
- Rowe, C. C., Ellis, K. A., Rimajova, M., Bourgeat, P., Pike, K. E., Jones, G., et al. (2010). Amyloid imaging results from the Australian Imaging, Biomarkers and Lifestyle (AIBL) study of aging. Neurobiol. Aging **31**, 1275 – 1283.
- Saegusa, T. and Shojaie, A. (2016). Joint estimation of precision matrices in heterogeneous populations. Electron. J. Stat. **10**, 1341–1392.
- Shaddox, E., Stingo, F. C., Peterson, C. B., Jacobson, S., Cruickshank-Quinn, C., Kechris, K., et al. (2018). A Bayesian approach for learning gene networks underlying disease severity in COPD. Statistics in Biosciences pages 1–27.
- Singh, V., Chertkow, H., Lerch, J. P., Evans, A. C., Dorr, A. E., and Kabani, N. J. (2006). Spatial patterns of cortical thinning in mild cognitive impairment and Alzheimer's disease. Brain **129**, 2885–2893.
- Sporns, O. and Zwi, J. D. (2004). The small world of the cerebral cortex. Neuroinformatics **2**, 145–162.
- Wang, H. (2012). Bayesian graphical lasso models and efficient posterior computation. Bayesian Analysis **7**, 771–790.
- Wang, H. (2015). Scaling it up: Stochastic search structure learning in graphical models. Bayesian Analysis **10**, 351–377.
- Wang, H. and Li, S. (2012). Efficient Gaussian graphical model determination under  $G$ -Wishart prior distributions. Electron. J. Stat. **6**, 168–198.
- Wang, T., Wang, K., Qu, H., Zhou, J., Li, Q., Deng, Z., et al. (2016). Disorganized cortical thickness covariance network in major depressive disorder implicated by aberrant hubs

- in large-scale networks. Scientific Reports **6**, 27964.
- Yao, Z., Zhang, Y., Lin, L., Zhou, Y., Xu, C., and Jiang, T. (2010). Abnormal Cortical Networks in Mild Cognitive Impairment and Alzheimer’s Disease. PLOS Comput. Biol. **6**, e1001006.
- Yuan, M. and Lin, Y. (2007). Model selection and estimation in the Gaussian graphical model. Biometrika **94**, 19–35.
- Zhu, Y., Shen, X., and Pan, W. (2014). Structural pursuit over multiple undirected graphs. J. Am. Stat. Assoc. **109**, 1683–1696.

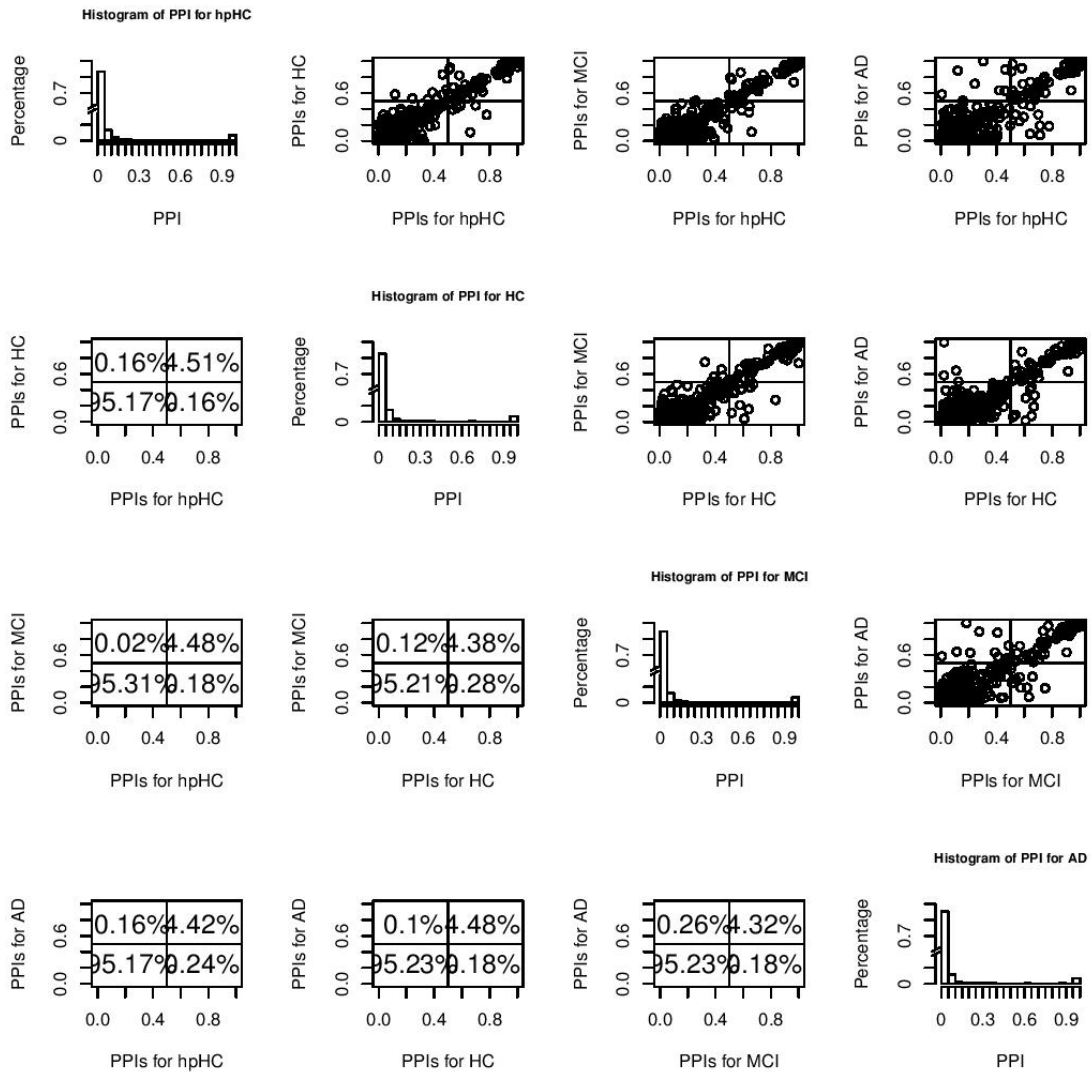


**Figure 1.** Case study results discussed in Section 4.3. PPIs across the 4 groups of subjects. Plots on the diagonal show histograms of the PPIs for the individual groups. We introduced a break in the y-axis to allow better visualization of the small PPIs. Off-diagonal plots show scatter plots of the PPIs, on the upper triangle plots, and percents of PPIs falling in each quadrant, in the lower triangle plots, for pairs of groups.

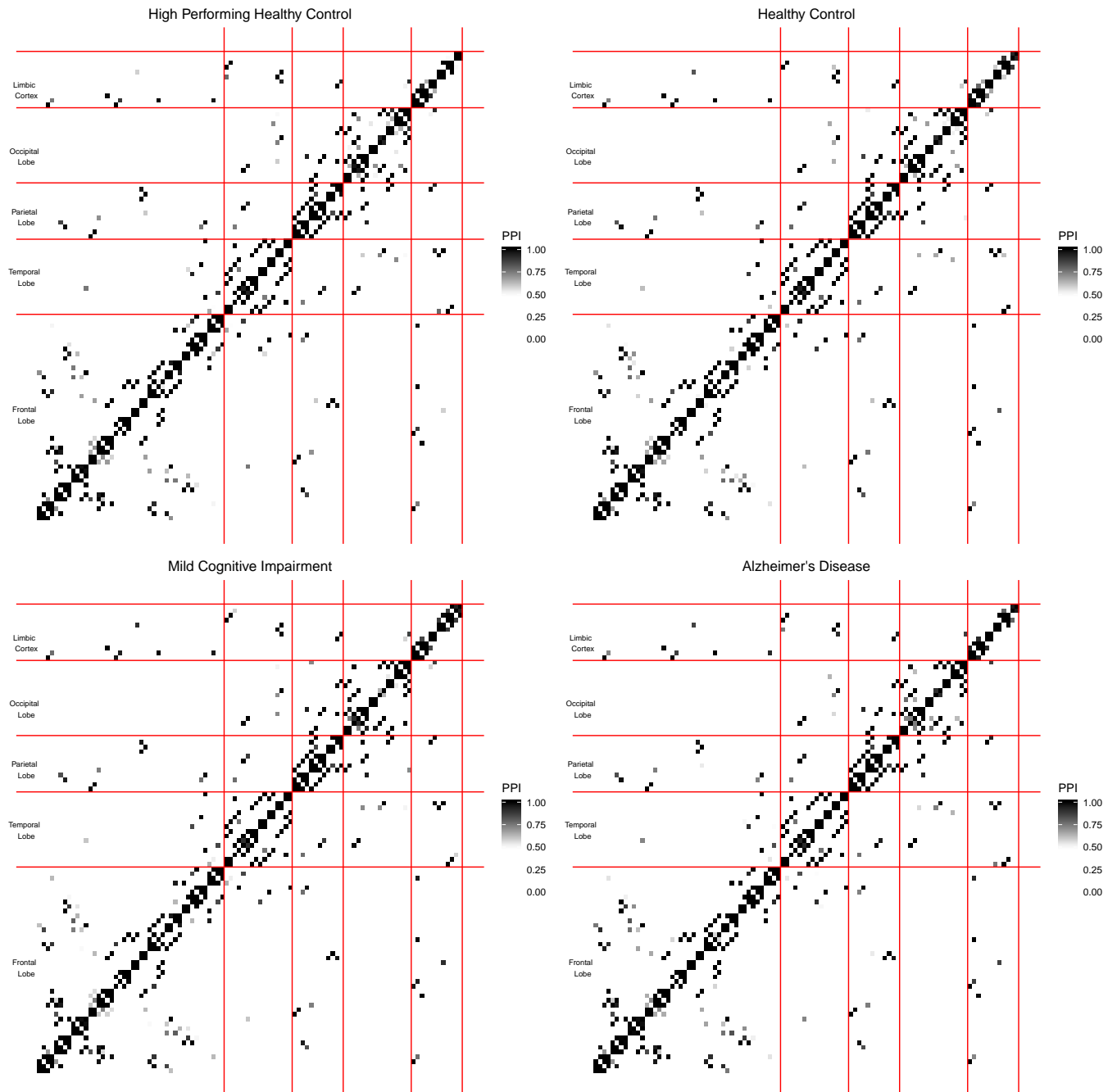


**Figure 2.** Case study results discussed in Section 4.3. Plot of the PPIs across the 4 groups of subjects. In each plot, ROIs are grouped within individual brain lobes.

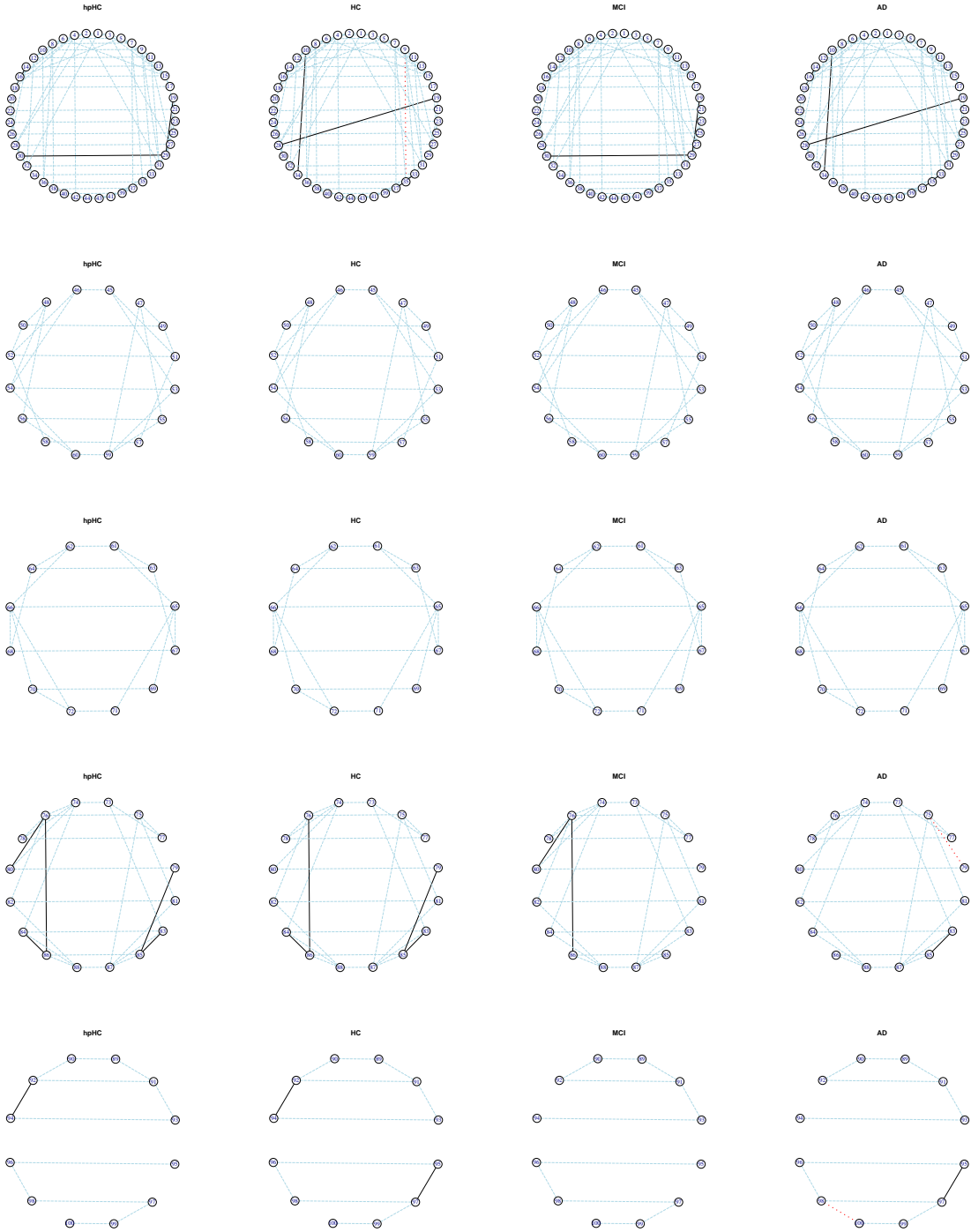


**Figure 3.** Case study results discussed in Section 4.3. Subnetworks corresponding to the frontal, temporal, parietal, occipital, and limbic lobes (from top to bottom), for the 4 groups of subjects.

All ROIs	hpHC	HC	MCI	AD	Frontal	hpHC	HC	MCI	AD
hpHC	231 (1)				hpHC	89 (1)			
HC	223	231 (3)			HC	86	91 (2)		
MCI	222	217	223 (1)		MCI	87	85	87 (0)	
AD	219	222	214	227 (3)	AD	86	89	85	89 (0)
Temporal	hpHC	HC	MCI	AD	Parietal	hpHC	HC	MCI	AD
hpHC	25 (0)				hpHC	19 (0)			
HC	25	25 (0)			HC	19	19 (0)		
MCI	25	25	25 (0)		MCI	19	19	19 (0)	
AD	25	25	25	25 (0)	AD	19	19	19	19 (0)
Occipital	hpHC	HC	MCI	AD	Limbic	hpHC	HC	MCI	AD
hpHC	30 (0)				hpHC	12 (0)			
HC	29	29 (0)			HC	12	13 (0)		
MCI	27	26	27 (0)		MCI	11	11	11 (0)	
AD	26	26	25	27 (1)	AD	11	12	11	13 (1)

**Table 1**

Case study results discussed in Section 4.3. Number of edges included per group and shared across groups in the networks for all ROIs of Supplementary Figure S2 and the lobe-specific networks of Figure 3. Diagonal values represent the number of edges selected in each group, with values in parenthesis representing the number of edges that are unique to that group. Off-diagonal values indicate the numbers of shared edges between pairs of groups.

		Fused	Separate	Joint	Linked	Fused	Separate	Joint	Linked	Fused	Separate	Joint	Linked	Fused	Separate	Joint	Linked
All	Fused	1486				1495				1345				1218			
Regions	Separate	167	168			175	175			181	181			185	185		
	Joint	578	168	670		576	175	679		534	181	652		587	185	688	
	Linked	229	142	215	231	229	147	218	231	222	160	221	223	226	165	223	227
	Fused	459				418				421				399			
Frontal Lobe	Separate	62	62			68	68			66	66			68	68		
	Joint	204	62	216		198	68	220		196	66	212		211	68	225	
	Linked	88	53	82	89	90	59	85	91	87	61	86	87	89	62	88	89
	Fused	73				76				66				65			
Temporal Lobe	Separate	23	23			20	20			24	24			24	24		
	Joint	45	23	48		49	20	50		46	24	47		49	24	50	
	Linked	25	22	24	25	25	19	25	25	25	22	25	25	25	23	25	25
	Fused	55				52				54				48			
Parietal Lobe	Separate	16	16			19	19			15	15			16	16		
	Joint	40	16	40		40	19	40		37	15	37		34	16	35	
	Linked	19	16	19	19	19	16	19	19	19	15	19	19	19	13	19	19
	Fused	97				104				89				75			
Occipital Lobe	Separate	22	22			27	27			25	25			23	23		
	Joint	49	22	52		56	27	56		46	25	46		48	23	48	
	Linked	30	22	29	30	29	23	29	29	27	23	27	27	27	22	27	27
	Fused	31				27				24				29			
Limbic Lobe	Separate	9	9			10	10			10	10			12	12		
	Joint	14	9	16		16	10	16		13	10	13		17	12	17	
	Linked	12	9	12	12	13	10	13	13	11	10	11	11	13	11	12	13
	Fused																

**Table 2**

Comparison of case study results discussed in Section 4.4. For each group and brain region, diagonal values represent the total number of edges using the specified method, and off diagonal values represent the number of edges the two methods have in common. Fused is the fused graphical lasso of Danaher et al. (2014), Separate is the separate Bayesian graph estimation with mixture priors of Wang (2015), emphJoint is the joint Bayesian estimation with mixture priors of Shaddox et al. (2018), and Linked is the proposed approach.



	All Edges						Differential Edges			
	TPR	FPR	MCC	AUC	Fr Loss	# edges	TPR	FPR	MCC	AUC
Fused graphical lasso	0.80 (0.01)	0.07 (0.003)	0.48 (0.01)	<b>0.97</b> (0.001)	0.065 (0.001)	461 (15.1)	0.74 (0.01)	0.14 (0.001)	0.11 (0.003)	0.24 (0.01)
Group graphical lasso	0.73 (0.01)	0.08 (0.003)	0.40 (0.005)	0.96 (0.001)	0.077 (0.001)	508 (16.3)	0.68 (0.02)	0.14 (0.004)	0.10 (0.003)	0.13 (0.004)
Separate estimation with mixture priors	0.17 (0.002)	0.0002 (3.0e-05)	0.40 (0.003)	0.89 (0.001)	0.099 (0.001)	31 (0.5)	0.16 (0.01)	0.01 (2.0e-04)	0.10 (0.01)	0.84 (0.01)
Joint estimation with mixture priors	0.57 (0.004)	0.03 (3.0e-04)	0.47 (0.003)	0.89 (0.002)	0.327 (0.003)	236 (1.6)	0.53 (0.02)	0.06 (0.001)	0.12 (0.004)	0.84 (0.01)
<b>Linked precision matrix approach</b>	0.43 (0.01)	0.0002 (2.6e-05)	<b>0.64</b> (0.004)	0.95 (0.001)	<b>0.057</b> (7.4e-04)	77 (1.1)	0.22 (0.01)	0.003 (9.9e-05)	<b>0.23</b> (0.019)	<b>0.87</b> (0.01)

**Table 3**

Performance summary across 25 simulated data sets. Comparison of true positive rate (TPR), false positive rate (FPR), Matthews correlation coefficient (MCC) and area under the ROC curve (AUC) for structure learning, and Frobenius loss (FL) for precision matrix estimation. The standard error of the mean is given in parentheses.